

Prospects and Strategies for Detecting Nonlinear Gravitational Wave Burst with Memory from Potential Merger Event SDSSJ1430+2303 by Pulsar Timing Arrays

Jie-Wen Chen, Yiqiu Ma * and Yan Wang †

¹Center for Gravitational Experiments, Hubei Key Laboratory of Gravitation and Quantum Physics, School of Physics, Huazhong University of Science and Technology, Wuhan, 430074, P. R. China

²Department of Astronomy, School of Physics, Huazhong University of Science and Technology, Wuhan, 430074, P. R. China

Accepted XXX. Received YYY; in original form ZZZ

ABSTRACT

The recently observed chirping signature in the light curves of Seyfert 1 galaxy SDSSJ1430+2303 could be explained by a late-inspiralling supermassive binary black hole (SMBBH) system in the galactic center, which will merge in the near future (or could have been merged already). For the merging SMBBH scenario, SDSSJ1430+2303 can be a source of nonlinear gravitational wave (GW) burst with memory (BWM), which may provide a promising target for future pulsar timing array (PTA) observations. In this work, we investigate the prospects for detecting the BWM signal from SDSSJ1430+2303 by the International PTA (IPTA) and FAST-PTA in the next 5 years. We firstly propose strategies on searching for this target signal, including the selection of millisecond pulsars (MSPs) and the distribution of observation time. Then we simulate PTA observations based on the proposed strategies and obtain the probability density functions of the network signal-to-noise ratio and parameter-estimation errors of the BWM signal, considering the uncertainties of parameters of the SMBBH and both white and red noises of the selected MSPs. Our result shows that although IPTA can marginally detect the BWM in 5 years, FAST-PTA can detect it with significantly higher confidence. Moreover, the achieved IPTA data is important in estimating the merger time of the SMBBH, when combined with the FAST-PTA data. This work can serve as a guidance for future PTA observations and multi-messenger studies on SDSSJ1430+2303 and similar systems.

Key words: Gravitational Wave Burst with Memory – Pulsar Timing Array – Observation Strategy

1 INTRODUCTION

The recent observations of Seyfert 1 galaxy SDSSJ143016.05+2303 (hereafter SDSSJ1430+2303) at various electromagnetic wavelengths, in particular at the optical and X-ray bands, reported periodically varying light curves with decreasing oscillation amplitude and period (Jiang et al. 2022). Although there could be other physical mechanisms (e.g., oscillations or instabilities of the AGN accretion disk (Jiang et al. 2022)), it is plausible that the observation signatures can be generated from a supermassive binary black hole (SMBBH) system in a highly eccentric orbit (see Figure 1). Moreover, this SMBBH scenario provides the predictions that can be further tested by the near future multi-messenger observations, since the fitted orbit evolution models show that this SMBBH is currently at its late inspiral stage and will merge in a few years or could have merged recently. Despite this merger event will occur too soon to be captured by the future space-borne gravitational wave (GW) detectors (e.g., LISA (Danzmann 1997; Amaro-Seoane et al. 2017), Taiji (Hu & Wu 2017) and TianQin (Luo et al. 2016)) and also the frequency band of its GWs is too low to be detected by using the current ground-based GW detectors (e.g., LIGO (Harry 2010; Aasi et al. 2015) and Virgo

(Acernese et al. 2014)), the nonlinear Christodoulou GW memory effect (Payne 1983; Blanchet & Damour 1992; Christodoulou 1991; Thorne 1992) can still have the chance to be detected by the pulsar timing arrays (PTAs) as pointed out by Jiang et al. (2022).

GW memory is a non-oscillatory contribution of the metric before and after the merger event (Favata 2009a,c; van Haasteren & Levin 2010; Pshirkov et al. 2010). The non-linear GW memory contributed by the GW stress-energy tensor is a manifestation of the nonlinearity of the Einstein’s gravitational theory. Detecting nonlinear GW memory effect can in principle provides a strong-field test of general relativity. The redshift of SDSSJ1430+2303 is estimated to be small (≈ 0.08), therefore the GW memory effect could be detected if SDSSJ1430+2303 is indeed an inspiralling SMBBH system. In particular, since there will be a SMBBH merger event in a few years as predicted by the orbit evolution models of the SMBBH, it would be very important to test this model by detecting the corresponding nonlinear GW memory.

Jiang et al. (2022) has pointed out that the GW burst with memory (BWM) effect is promising and can be detected by PTAs. The signal-to-noise ratio (S/N) is estimated to be ≈ 1 based on a simple observation strategy – biweekly observation of 20 millisecond pulsars (MSPs) with a timing precision 100 ns for a duration of 5 years. Hence it is important to give a prospective investigation for detecting the BWM signal by the recent-future PTA projects, considering

*Email: myqphy@hust.edu.cn

†Email: ywang12@hust.edu.cn

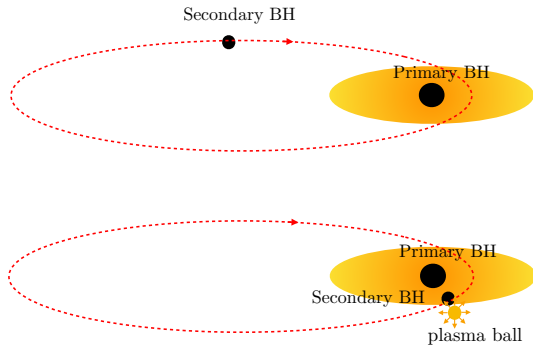


Figure 1. Schematic illustration of the proposed model for SDSSJ1430+2303, a highly eccentric supermassive binary black hole system with black hole masses $M_1 \approx 3 \times 10^8 M_\odot$, $M_2 \approx 6 \times 10^7 M_\odot$. The time varying light curves result from the electromagnetic radiation from the plasma ball brought by the collision of the secondary black hole with the accretion disk of the primary black hole.

more realistic performance of the radio telescopes and characteristics of the MSPs. Currently, the global effort of PTA observation is carried out under the umbrella of the International PTA (IPTA) consortium (Hobbs et al. 2010; Manchester 2013), which consists of four regional members — the Parks PTA (PPTA) (Manchester et al. 2013; Hobbs 2013), the North American Nanohertz Observatory for GWs (NANOGrav) (McLaughlin 2013; Ransom et al. 2019), the European PTA (EPTA) (Kramer & Champion 2013) and the Indian PTA (InPTA) (Joshi et al. 2018). The IPTA has accumulated pulsar time of arrivals (TOAs) data for more than ten years, offering 65 stable MSPs among which 15 have a timing precision below $1 \mu\text{s}$ (Perera et al. 2019a). Furthermore, the Five-hundred-meter Aperture Spherical radio Telescope (FAST) is now the largest single-dish radio telescope and is expected to provide unprecedented high precision measurement of pulsar time of arrivals (Nan et al. 2011; Hobbs et al. 2019). FAST will play an important role in the future Chinese PTA (CPTA) project (Lee 2016). The purpose of this work is to investigate the prospects and provide strategies for detecting the BWM signal from SDSSJ1430+2303 by IPTA observations and FAST-PTA observations.

The rest of the article is organized as follows. In section 2, we briefly introduce the BWM signal and the timing residual template induced by it. In section 3, we discuss the details of the observation strategies for detecting the BWM by PTA. In section 4, we analyze the PDFs of the network S/Ns and parameter-estimation errors, to test and further select the strategies, and also to investigate the prospects for detecting the GW signal. This article is concluded in section 5.

2 TIMING RESIDUAL INDUCED BY THE NONLINEAR GW MEMORY

GW memory effect, as briefly mentioned in the Introduction, is a non-oscillatory permanent distortion of the spacetime metric. This memory effect is caused by the DC changes in the time derivatives of the source multiple moments (Favata 2009a,c). The non-linearity in the relativistic gravitational field equations indicates that the gravitational wave itself can carry time-varying energy momentum thereby can also contribute to the GW memory effect (Thorne 1992; Favata

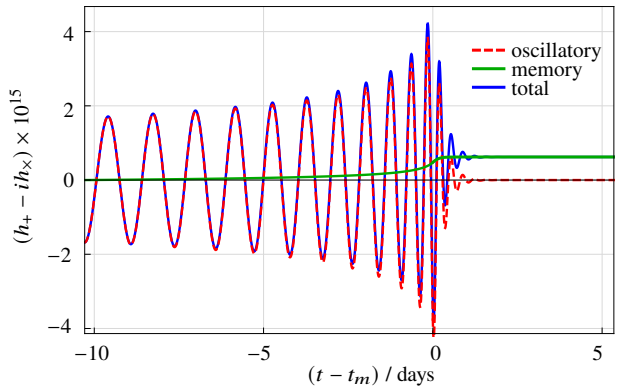


Figure 2. Illustration for the waveform of the GW BWM from SDSSJ1430+2303. In this case, the masses of the two black holes are taken as $3 \times 10^8 M_\odot$ and $6 \times 10^7 M_\odot$ (Jiang et al. 2022), ι is taken as 90° . The effective-one-body and quasi-normal mode waveforms are matched at the distance $3GM/c^2$ (Favata 2009c), with M being the total mass of the SMBBH.

2009a). This phenomenon has been independently found by Payne (1983), Blanchet & Damour (1992) and Christodoulou (1991). It is intriguing and important since it can be used to test the general relativity in the strong-field regime and may be related to other topics relevant to the fundamental physics. It has been proposed that the BWM effect can be detected by high precision measurement of the pulsar TOAs for a set of MSPs in a PTA (van Haasteren & Levin 2010; Pshirkov et al. 2010), and its upper limit has been improved over the years (Arzoumanian et al. 2015; Wang et al. 2015; Aggarwal et al. 2020).

The DC GW memory is given by Favata (2009c,b):

$$h_+^{\text{mem}}(t) = \frac{\sin^2 \iota (17 + \cos^2 \iota)}{384\pi R} \int_{-\infty}^t |I_{22}^{(3)}(t')|^2 dt', \quad (1)$$

where we adopt a standard choice of polarization tensor in which $h_\times^{\text{mem}}(t) = 0$ (Favata 2009c,b), $I_{22}^{(3)}(t)$ is the third time derivative of the source mass moment for the $l = |m| = 2$ mode, R is the luminosity distance between the source and the detector and ι is the inclination angle. For the merger event of SDSSJ1430+2303, using the parameters estimated by Jiang et al. (2022), the GW memory effect around the merger time is plotted in Figure 2. This waveform is obtained by matching the effective-one-body waveform (which extends the Post-Newtonian (PN) equations of motion to the plunge region by mapping the PN two-body description to a one-body problem in a parametrized deformed Schwarzschild metric (Damour 2008)) and the ringdown waveform (see Favata 2009c,b; Berti et al. 2006, for details).

The memory metric perturbation in Equation 1 has a transient growing part which lasts for a timescale $[1.45 \text{ mHz} \times (2 \times 10^6 M_\odot / M)]^{-1} \approx 1 \text{ day}$ (Favata 2009c) (as shown in Figure 2), where $M \approx 3 \times 10^8 M_\odot$ is the total mass of the SMBBH in SDSSJ1430+2303. This is much shorter than the typical cadences (2 – 4 weeks) of PTA observations (Perera et al. 2019a). Therefore we can use the Heaviside step function Θ to approximate the above memory waveform as

$$h_+^{\text{mem}}(t) = \Theta(t - t_m)h, \quad (2)$$

where t_m is the merger time and h is the strain amplitude of the GW memory. Thus, for the I_{th} MSP in a PTA, the timing residual induced by the GW memory can be approximately written as (Pshirkov et al.

2010; van Haasteren & Levin 2010)

$$s_I(t) = (t - t_m)\Theta(t - t_m)F_I h, \quad (3)$$

where $F_I = (F_{I,+} \cos 2\psi - F_{I,\times} \sin 2\psi)$ (Taylor et al. 2016), ψ is the GW polarization angle, and

$$F_{I,+} = \frac{1}{4(1 - \cos \theta)} \left[(1 + \sin^2 \delta) \cos^2 \delta_I \cos(2\alpha - 2\alpha_I) - \sin 2\delta \sin 2\delta_I \cos(\alpha - \alpha_I) + \cos^2 \delta (2 - 3 \cos^2 \delta_I) \right], \quad (4)$$

$$F_{I,\times} = \frac{1}{2(1 - \cos \theta)} \left[-\sin \delta \cos^2 \delta_I \sin(2\alpha - 2\alpha_I) + \cos \delta \sin 2\delta_I \sin(\alpha - \alpha_I) \right],$$

are the antenna pattern functions, with $\cos \theta = \cos \delta \cos \delta_I \cos(\alpha - \alpha_I) + \sin \delta \sin \delta_I$. Here $\alpha = 14^{\text{h}}30^{\text{m}}$ and $\delta = +23^{\circ}03'$ are the right ascension (RA) and declination (DEC) of the source, and the α_I, δ_I are the RA and DEC of the MSP, respectively. The probability density functions (PDFs) of t_m and h are given by Jiang et al. (2022), where they consider two possible SMBBH 4.5PN orbit models that are obtained from the fits based on the optical observations (Model-1) and the optical + X-ray joint observations (Model-2). Model-1 predicts a expected merger time around 2023-2024, while Model-2 predicts that the merger event is likely to occur within several months from now. For Model-2, if the initial observation epoch ($t_{I,i}$) is later than the merger time t_m , the template in Equation 3 should be modified to

$$s_I(t) = (t - t_{I,0})\Theta(t - t_m)F_I h, \quad (5)$$

where $t_{I,0} = \text{Max}[t_m, t_{I,i}]$.

3 OBSERVATION STRATEGY

An optimal observation strategy for detecting the nonlinear BWM effect consists of a selection of MSPs and a distribution of observation time that maximize the network S/N

$$\rho^2 = \sum_{I=1}^{N_P} \rho_I^2 = \sum_{I=1}^{N_P} \sum_{n=1}^{N_I} \frac{s_I^2(t_n)}{\sigma_{I,W}^2 + \sigma_{I,R}^2(t_n)} \approx \sum_{I=1}^{N_P} \int_{t_{I,i}}^{t_{I,i}+T_I} \frac{dt}{\Delta T_I} \frac{s_I^2(t)}{\sigma_{I,W}^2 + \sigma_{I,R}^2(t)}. \quad (6)$$

Here, the N_P is the number of MSPs in the PTA, ρ_I is the individual S/N for the I_{th} MSP. $\sigma_{I,W}$ and $\sigma_{I,R}$ are the root-mean-square (r.m.s.) of white noise and effective r.m.s. of red noise (Shannon & Cordes 2010), respectively. $t_{I,i}, T_I$ and ΔT_I are the initial date, span and cadence of the observation, respectively. For simplicity, we assume that the cadence is a constant $\Delta T_I = T_I/(N_I - 1)$ in this work, where N_I is the total number of data points for this MSP.

The noises $\sigma_{I,W}$ and $\sigma_{I,R}$ will be discussed in subsection 3.1. The details of the observation strategy will be demonstrated in subsection 3.2 and the results will be discussed in subsection 3.3.

3.1 Noise Evaluation

• **White noise** — The IPTA DR2 (Perera et al. 2019a) has released $\sigma_{I,W}$ for 65 MSPs, as is listed in column 2 of Table 1, some of which are within the sky area accessible by FAST ($-14^{\circ} < \text{DEC} < 66^{\circ}$).

The white noise r.m.s. $\sigma_{I,W}$ for these MSPs, when observed by FAST, can be estimated as follows.

For a specific MSP, the white noise consists of the following jitter noise ($\sigma_{I,j}$) and radiometer noise ($\sigma_{I,r}$),

$$\sigma_{I,j} = 0.2W_I \sqrt{\frac{P_I}{\Delta T_I}}; \quad \sigma_{I,r} = \frac{W_I T_{\text{sys}}}{GS_I \sqrt{2\Delta f \Delta T_I}} \sqrt{\frac{W_I}{P_I - W_I}}. \quad (7)$$

The total white noise $\sigma_{I,W} = \sqrt{\sigma_{I,j}^2 + \sigma_{I,r}^2}$. Here, the P_I, W_I and ΔT_I are the spin period, the pulse width and the integration time of each data point, respectively. S_I is the flux density of the MSP. In this work, ΔT_I is simply assumed to be a constant for a specific MSP, so that the total integration time allocated to the MSP is $\tau_I = N_I \Delta T_I$. The $G, T_{\text{sys}}, \Delta f$ are the gain, the system temperature, and the receiver's bandwidth of the telescope, respectively. The corresponding values for FAST is listed in Table 2. As in Hobbs et al. (2019), we ignore the dependence of G and T_{sys} on the zenith angle and simply set $G = 16.0 \text{ K Jy}^{-1}$ and $T_{\text{sys}} = 20 \text{ K}$ in this work. Equation 7 implies that $\sigma_{I,W} \propto \Delta \tau_I^{-1/2}$, and in practical measurements, $\Delta \tau_I$ is required to be not smaller than 5 min (Rathnasree & Rankin 1995) and is typically $\approx 10 - 30 \text{ min}$. To calculate the r.m.s. of white noises for those MSPs by FAST, we also list the MSP parameters S_I, P_I and W_I in columns 3-5 of Table 1, and show the resulting white noise for $\Delta T_I = 5 \text{ min}$ in column 6.

• **Red noise** — The time correlated pattern observed in timing residuals is usually referred to as spin noise or timing noise. It has a red power spectral density and can arise from the spin irregularity of the pulsar that may be caused by the varying coupling between the crust and the internal core of the neutron star (Wang 2015). The typical strength of the timing noise in the MSP is orders of magnitude weaker than the ones in the normal pulsar or magnetar. However, it can appear in the long term high precision measurements of TOAs of MSPs and has adverse impact on the detection of GW by delaying the expected detection time (Siemens et al. 2013). As the reason that will become clear later, adding red noise intrinsic in the MSPs in our analysis for FAST is crucial for obtaining a realistic observation strategy. Here we adopt the model to estimate the level of the red noise given by Shannon & Cordes (2010):

$$\ln \frac{\sigma_{I,R}}{1\mu\text{s}} \in N \left[\ln \frac{\tilde{\sigma}_{I,R}}{1\mu\text{s}}, \delta^2 \right], \quad (8)$$

where

$$\frac{\tilde{\sigma}_{I,R}}{1\mu\text{s}} = C \left(\frac{P_I}{1\text{s}} \right)^{-\alpha-2\beta} \left(\frac{\dot{P}_I}{10^{-15}} \right)^{\beta} \left(\frac{t - t_{I,i}}{1\text{yr}} \right)^{\gamma}, \quad (9)$$

with $\ln C \in N[-1.2, 1.25^2]$, $\alpha \in N[-0.9, 0.2^2]$, $\beta \in N[0.8, 0.05^2]$, $\gamma \in N[2.3, 0.15^2]$ and $\delta \in N[1.1, 0.05^2]$ (Lam et al. 2016). We find that for the observations with $t - t_{I,i} \leq 10 \text{ years}$, the above model can be simplified as

$$\sigma_{I,R}(t) \in \tilde{\sigma}_{I,R} 10^{N[0, \delta_I^2]} = \tilde{\sigma}_{I,R,1 \text{ yr}} \left(\frac{t - t_{I,i}}{1 \text{ yr}} \right)^{2.3} 10^{N[0, \delta_I^2]}, \quad (10)$$

where $\tilde{\sigma}_{I,R}$ is the expectation value of the red noise, and δ_I is the parameter of uncertainty. The expected 1-year red noise $\tilde{\sigma}_{I,R,1 \text{ yr}}$ and the parameter δ_I for the MSPs are listed in columns 8-9 of Table 1.

3.2 MSP selection and observation time allocation

For each selected MSP, the observation time to be determined includes 4 free parameters: $T_I, t_{I,i}, \tau_I$ and ΔT_I (or alternatively $\Delta \tau_I$,

Table 1. Parameters of 65 IPTA MSPs. Column 2 shows the measured $\sigma_{I,W}$ given by IPTA DR2 (Perera et al. 2019a); columns 3-5 give the measured S_I at 1.4 GHz, P_I , and W_I (at 50% intensity), respectively, where the data are cited from IPTA DR2 (Perera et al. 2019a), EPTA 2016 results (Desvignes et al. 2016), PPTA DR2 (Kerr et al. 2020), NANOGrav 12.5-year results (Alam et al. 2020a,b), the ATNF Pulsar Catalogue (Manchester et al. 2005) (<http://www.atnf.csiro.au/research/pulsar/psrcat/>) and the references therein; column 6 illustrates the evaluated $\sigma_{I,W}$ by FAST with $\Delta\tau_I = 5$ min, from Equation 7; column 7 lists the observed \dot{P}_I cited from the ATNF Pulsar Catalogue; columns 8-9 show parameters $\hat{\sigma}_{I,R,1\text{yr}}$ and δ_I in Equation 10; columns 10 shows T_I^* given by Equation 13 for FAST-PTA, and columns 11 shows T_I^* for IPTA, assuming that the white noises in column 2 are measured at $\Delta\tau_I = 20$ min for all MSPs.

MSP name	$\sigma_{I,W,\text{IPTA}}$ (ns)	$S_{I,1.4}$ (mJy)	P_I (ms)	$W_{I,50}$ (ms)	$\sigma_{I,W,5\text{min,FAST}}$ (ns)	\dot{P}_I (10^{-20})	$\hat{\sigma}_{I,R,1\text{yr}}$ (ns)	δ_I	$T_{I,\text{FAST}}^*$ (yr)	$T_{I,\text{IPTA}}^*$ (yr)
J0023+0923	1340	0.32	3.050	–	–	1.14	1.93	0.88	–	26.6
J0030+0451	1480	1.12	4.856	0.8	1034	1.02	1.28	0.86	21.1	33.3
J0034–0534	4190	0.61	1.877	0.65	2005	0.50	1.40	0.91	27.0	50.3
J0218+4232	7010	0.9	2.323	1.03	2669	7.74	10.8	0.90	12.6	25.9
J0340+4130	5160	0.54	3.299	–	–	0.70	1.23	0.88	–	58.3
J0613–0200	1140	2.3	3.062	0.462	366	0.96	1.68	0.88	11.9	26.4
J0621+1002	6570	1.9	28.854	0.69	1361	4.73	1.25	0.79	24.0	64.3
J0645+5158	570	0.3	8.853	0.26	477	0.49	0.46	0.83	23.5	34.3
J0751+1807	3000	3.2	3.479	0.7	553	0.78	1.30	0.88	15.9	44.9
J1012+5307	1910	3.2	5.256	0.85	771	1.71	1.82	0.86	15.9	31.9
J1022+1001	1970	6.1	16.453	0.972	1443	4.33	1.72	0.81	21.4	33.1
J1024–0719	1710	1.5	5.162	0.521	524	1.86	1.97	0.86	13.0	29.4
J1640+2224	770	2.0	3.163	0.22	162	0.28	0.61	0.88	13.0	34.6
J1643–1224	2550	4.8	4.622	0.314	251	1.85	2.13	0.86	9.1	33.8
J1713+0747	210	10.2	4.570	0.11	86	0.85	1.15	0.86	7.5	14.9
J1738+0333	1380	0.7	5.850	0.43	582	2.41	2.22	0.85	12.9	25.4
J1741+1351	460	0.9	3.747	0.16	148	3.02	3.63	0.87	5.7	12.7
J1744–1134	730	3.1	4.075	0.137	103	0.89	1.30	0.87	7.7	24.3
J1832–0836	1860	1.18	2.719	0.058	40	0.83	1.62	0.89	4.6	33.2
J1843–1113	710	0.1	1.846	0.25	2528	0.96	2.38	0.91	23.7	18.5
J1853+1303	1310	0.43	4.092	0.59	1501	0.87	1.26	0.87	24.9	31.8
J1857+0943	1160	5.0	5.362	0.518	446	1.78	1.86	0.85	12.4	25.4
J1903+0327	2110	1.3	2.150	–	–	1.88	3.68	0.90	–	24.5
J1910+1256	1420	0.56	4.984	0.14	157	0.97	1.20	0.86	9.5	33.6
J1911–1114	4300	0.5	3.626	0.18	244	1.40	2.01	0.87	9.2	43.5
J1911+1347	1090	0.86	4.626	0.089	79	1.69	1.97	0.86	5.7	24.1
J1918–0642	1800	1.36	7.646	0.66	767	2.57	1.94	0.84	15.4	30.2
J1923+2515	2250	0.28	3.788	0.38	1187	0.96	1.45	0.87	21.2	37.8
J1939+2134	240	13.2	1.558	0.038	17.4	10.5	18.3	0.92	1.1	4.7
J1944+0907	2220	2.6	5.185	0.5	446	1.73	1.85	0.86	12.4	33.8
J1949+3106	4610	0.2	13.138	–	–	9.39	3.75	0.82	–	34.2
J1955+2908	3200	1.1	6.133	0.65	784	2.97	2.54	0.85	13.9	34.5
J2010–1323	2530	1.6	5.233	0.28	257	0.48	0.66	0.86	15.3	56.3
J2017+0603	720	0.5	2.896	–	–	0.80	1.51	0.88	–	22.6
J2019+2425	9640	0.1	3.934	0.3	2210	0.70	1.09	0.87	31.4	80.6
J2033+1734	13650	0.3	5.949	0.16	267	1.11	1.18	0.85	12.1	90.5
J2043+1711	630	0.21	2.380	–	–	0.52	1.22	0.89	–	23.4
J2145–0750	1730	8.9	16.052	0.337	494	2.98	1.30	0.81	15.2	35.4
J2214+3000	1670	0.5	3.199	0.23	360	1.47	2.28	0.88	10.4	27.3
J2229+2643	4280	0.9	2.978	0.58	887	0.15	0.39	0.88	33.0	88.5
J2302+4442	5820	1.2	5.192	0.34	342	1.39	1.56	0.86	11.9	55.4
J2317+1439	870	4	3.445	0.4	286	0.24	0.51	0.87	18.0	39.1
J2322+2057	6740	0.03	4.808	0.3	6587	0.97	1.23	0.86	47.8	199
J0437–4715	110	149	5.757	0.14	–	5.73	4.48	0.85	–	6.2
J0610–2100	4880	0.4	3.816	0.57	–	1.23	1.76	0.87	–	48.7
J0711–6830	1440	3.2	5.491	1.09	–	1.49	1.60	0.85	–	29.8
J0900–3144	3210	3.8	11.11	0.80	–	4.89	2.51	0.82	–	34.8
J0931–1902	3690	0.84	4.638	0.45	–	0.36	0.57	0.86	–	70.3
J1045–4509	3190	2.7	7.474	0.84	–	1.77	1.47	0.84	–	43.7
J1455–3330	4120	1.2	7.987	0.80	–	2.43	1.80	0.84	–	44.8
J1600–3053	920	2.5	3.598	0.094	–	0.95	1.48	0.87	–	25.4
J1603–7202	1580	3.1	14.84	1.21	–	1.56	0.82	0.81	–	41.5
J1614–2230	1380	1.11	3.151	0.30	–	0.96	1.65	0.88	–	28.9
J1721–2457	12210	0.6	3.497	0.58	–	0.55	0.98	0.87	–	93.5
J1730–2304	1570	3.9	8.123	0.965	–	2.02	1.54	0.84	–	31.5

Table 1. — continued.

MSP name	$\sigma_{I,W,IPTA}$ (ns)	$S_{I,1.4}$ (mJy)	P_I (ms)	$W_{I,50}$ (ms)	$\sigma_{I,W,5min,FAST}$ (ns)	\hat{P}_I (10^{-20})	$\hat{\sigma}_{I,R,1yr}$ (ns)	δ_I	$T_{I,FAST}^*$ (yr)	$T_{I,IPTA}^*$ (yr)
J1732–5049	2720	1.3	5.313	0.29	–	1.42	1.56	0.85	–	39.8
J1747–4036	4790	1.55	1.646	–	–	1.31	3.31	0.91	–	36.7
J1751–2857	2850	0.1	3.915	0.25	–	1.12	1.60	0.87	–	38.4
J1801–1417	2760	0.2	3.625	0.60	–	0.53	0.93	0.87	–	50.1
J1802–2124	2760	0.8	12.65	0.37	–	7.26	3.13	0.82	–	29.6
J1804–2717	3720	0.4	9.343	1.55	–	4.09	2.45	0.83	–	37.4
J1824–2452A	570	2.0	3.054	0.97	–	1.62	2.55	0.88	–	16.3
J1909–3744	190	2.1	2.947	0.044	–	1.40	2.32	0.88	–	10.5
J2124–3358	2890	3.6	4.931	0.52	–	2.06	2.22	0.86	–	35.0
J2129–5721	980	1.1	3.726	0.26	–	2.09	2.72	0.87	–	20.0

 Table 2. The telescope instrumental parameters for FAST (Jiang et al. 2020); <https://fast.bao.ac.cn/cms/article/97/>.

parameters	values
G	11.0 – 16.0 K Jy ⁻¹
T_{sys}	19 – 27 K
band	1.4 GHz
Δf	400 MHz

since $\Delta\tau_I = \tau_I / (T_I / \Delta t_I + 1)$. Note that designing the observation strategy concerns a complicated process. The details of the process can be summarised as the following steps.

Step 1-Selection of $\Delta\tau_I$ — The integration time of each data point $\Delta\tau_I$ affects ρ_I , as well as the network S/N ρ , by determining the white noise level of the MSP. An optimal strategy requires a large ρ_I^2 / τ_I , which is

$$\frac{\rho_I^2}{\tau_I} = \frac{1}{N_I} \sum_{n=1}^{N_I} \frac{s_I^2(t_n)}{5 \min \cdot \sigma_{I,W,5min}^2 + \sigma_{I,R}^2(t_n) \Delta\tau_I}, \quad (11)$$

according to Equation 7, where $\sigma_{I,W,5min}$ is the white noise with $\Delta\tau_I = 5$ min. To yield a maximum ρ_I^2 / τ_I in the presence of red noise, $\Delta\tau_I$ should contain the minimum value 5 min. Therefore, in the following analyses, $\Delta\tau_I = 5$ min will be adopted as a preliminary selection, then its adjustment will be discussed in Step 6.

Step 2-Distribution of T_I — Generally speaking, ρ_I grows as the observation span T_I increases. However, at the late observation stage when the red noise dominates, the S/N will be saturated. This fact can be seen by substituting Equation 5 into Equation 6, which leads to:

$$\rho_I^2 \propto \int_{t_{i,1}}^{t_{i,1}+T_I} dt \frac{(t - t_{I,0})^2 \Theta(t - t_m)}{\sigma_{I,W}^2 + \sigma_{I,R}^2(t)}. \quad (12)$$

As mentioned above, $\sigma_{I,W}$ is independent from the span, while $\sigma_{I,R}(t) \propto (t - t_{I,0})^{2.3}$, if we estimate $\sigma_{I,R}$ as its expected value $\hat{\sigma}_{I,R}$ in Equation 10. Therefore, one can expect that: at the early observation stage, the white noise dominates over the red one and the S/N increases as the span T_I becomes larger; at the late stage, the red noise dominates and the S/N converges. To characterise this S/N convergence at the late stage, we define the S/N growing time scale

$$T_I^* = 1 \text{ yr} \times \left(\frac{3\sigma_{I,W,5min}^2}{1.6\hat{\sigma}_{I,R,1yr}^2} \right)^{\frac{1}{4.6}}, \quad (13)$$

by $\sigma_{I,W,5min}^2 \sim \sigma_{I,R}^2(t)$ at $t = T_I^* + t_{I,i}$. This result is based on the simple assumption that h_+^{mem} is non-zero at the beginning of the observation (i.e. $t_{I,i} \geq t_m$).

In a 5-year PTA observation, the span for a specific MSP T_I should

be designed to be no larger than T_I^* (i.e. $T_I = \text{Min}[T_I^*, 5 \text{ yr}]$), otherwise the observation during the excess span has little contribution to ρ_I . The values of T_I^* for FAST-PTA and IPTA are listed in columns 10 and 11 of Table 1, where we assume that the IPTA white noises in column 2 are measured with $\Delta\tau_I = 20$ min for all MSPs for simplicity.

Step 3-Selection of $t_{I,i}$ — To probe the BWM signal from SDSSJ1430+2303, the PTA observation is expected to start as early as possible, hence we take $t_{I,i} = 2022.3$ (mid-April of the year 2022) for most MSPs. However, for some specific MSPs, $t_{I,i}$ should be chosen differently for the following reason. In the Model-1 given by Jiang et al. (2022), the merger time t_m may be later than the date 2023.4 with a considerable probability. For the MSPs with $T_I^* \leq 1$ year (e.g. J1939+2134 with $T_I^* = 1.1$ yr in FAST-PTA, as shown in Table 1), it is possible that there are no BWM signals during most of the spans, if $t_{I,i} = 2022.3$ is taken. Therefore, we should delay the initial dates of observation for these MSPs.

In general, two cases are desired in observations: (i) t_m resides in the observation time range $[t_{I,i}, t_{I,i} + T_I]$, so that it can be measured (see subsection 4.2 for details); (ii) $t_{I,i} > t_m$, i.e. the BWM signal is non-zero initially, which leads to the largest ρ_I . Therefore, $t_{I,i}$ should be selected that both the cases can happen with significant probabilities. As a result, for the MSPs with $T_I^* \leq 1$ yr, $t_{I,i}$ is suggested to be around the date 2023.4, which is the moment that t_m takes the peaked value of PDF in Model-1 (Jiang et al. 2020). Finally, we notice that the above selection of $t_{I,i}$ will not affect ρ_I in Model-2, in which the case (ii) above is satisfied with probability ≈ 1 .

Step 4-MSP selection — The ρ_I depends on the antenna pattern function, sky location and noise level of the MSP. As an example, in Figure 3, we plot the antenna pattern function and the sky locations of the MSPs in the FAST sky, and make the noise inverse to the size of the stars. In the following, we will select MSPs considering these factors. Supposing all MSPs are observed during their efficient spans $T_I \leq T_I^*$, a MSP with a larger ρ_I^2 / τ_I should have a higher priority to be chosen. Considering the uncertainties of ψ and $\sigma_{I,R}$, we assume $\psi \in U[0, \pi]$ and take $\sigma_{I,R} = \hat{\sigma}_{I,R}$, then we define the priority parameter p_I for MSP selection as:

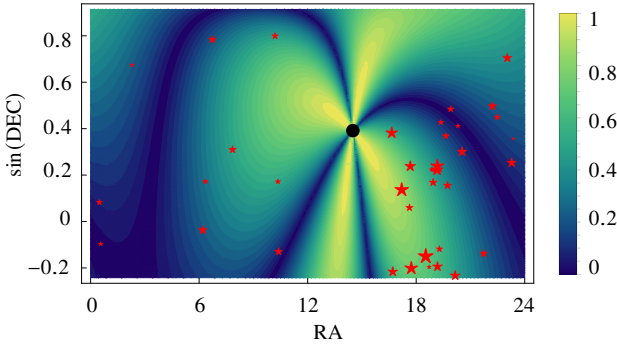
$$p_I = \frac{F_{I,+}^2 + F_{I,\times}^2}{N_I} \sum_{n=1}^{N_I} \frac{(t_n - t_{I,0})^2 \Theta(t_n - t_m)}{\sigma_{I,W}^2 + \hat{\sigma}_{I,R}^2} \propto \frac{\hat{\rho}_I^2}{\tau_I}, \quad (14)$$

where $\hat{\rho}^2$ is the ψ -averaged ρ^2 . For a specific telescope, the MSP with a larger p_I has a greater priority in observation. p_I computed and assigned to each MSPs for both FAST-PTA and IPTA are listed in Table 3.

Step 5-Distribution of τ_I — For a fixed total integration time

Table 3. Selected 20 MSPs with largest p_I and their parameters for a 5-year FAST-PTA (left) and a 5-year IPTA (right) observations started at 2022.3, respectively. The default values of span and initial date are $T_I = 5$ yr and $t_{I,i} = 2022.3$.

priority (FAST)	MSP name	$\overline{p_I}$ Max[p_I]	T_I (yr)	$t_{I,i}$	$\overline{\tau_I}$ Min[τ_I]	priority (IPTA)	MSP name	$\overline{p_I}$ Max[p_I]	T_I (yr)	$t_{I,i}$	$\overline{\tau_I}$ Min[τ_I]
1	J1832-0836	1	4.6	–	1	1	J1713+0747	1	–	–	1
2	J1713+0747	0.57	–	–	1.76	2	J1909-3744	0.40	–	–	2.48
3	J1911+1347	0.36	–	–	2.81	3	J1939+2134	0.26	4.7	–	3.92
4	J1744-1134	0.30	–	–	3.30	4	J1741+1351	0.20	–	–	5.11
5	J1939+2134	0.28	1.1	2023.4	3.53	5	J1640+2224	0.086	–	–	11.7
6	J1640+2224	0.20	–	–	4.96	6	J1824-2452A	0.072	–	–	13.8
7	J1741+1351	0.15	–	–	6.64	7	J1744-1134	0.063	–	–	15.9
8	J1910+1256	0.12	–	–	8.58	8	J1843-1113	0.051	–	–	19.6
9	J1643-1224	0.065	–	–	15.5	9	J0645+5158	0.050	–	–	19.9
10	J1911-1114	0.037	–	–	26.8	10	J2043+1711	0.042	–	–	24.0
11	J2033+1734	0.026	–	–	38.5	11	J1600-3053	0.040	–	–	24.9
12	J2010-1323	0.023	–	–	44.4	12	J2017+0603	0.034	–	–	29.8
13	J1857+0943	0.015	–	–	64.7	13	J0437-4715	0.032	–	–	31.3
14	J1738+0333	0.012	–	–	81.9	14	J1911-1347	0.024	–	–	41.9
15	J1944+0907	0.012	–	–	84.9	15	J1857+0943	0.022	–	–	45.5
16	J1024-0719	0.011	–	–	94.2	16	J1738+0333	0.021	–	–	48.0
17	J2302+4442	0.0098	–	–	102	17	J1614-2230	0.020	–	–	50.2
18	J2214+3000	0.0083	–	–	121	18	J1853+1303	0.018	–	–	55.5
19	J0645+5158	0.0075	–	–	133	19	J1910+1256	0.014	–	–	71.2
20	J1012+5307	0.0062	–	–	162	20	J1730-2340	0.012	–	–	81.7

**Figure 3.** Illustration for the antenna pattern function ($|F_I|$) of MSPs in the FAST sky. Here $|F_I|$ is illustrated by the brightness, and the brighter region represents larger $|F_I|$, hence stronger signal. The sky locations of MSPs are marked by red stars with sizes referring to the noise levels. Larger stars means MSPs with smaller noise $\sqrt{\sigma_{I,W}^2 + \sigma_{I,R}^2}$. The black point marks the location of SDSSJ1430+2303. In the presented case, the noise level is evaluated based on FAST-PTA, assuming $\psi = 22.5^\circ$, $\sigma_{I,R} = \hat{\sigma}_{I,R}$, and $t - t_{I,i} = 5$ yr

$\tau = \sum_{I=1}^{N_p} \tau_I$, different distribution strategies of τ_I among all MSPs will yield different values of ρ and different distributions of ρ_I . The distribution strategy should be taken in the way to avoid the situation that the network S/N is dominated by one or a few MSP(s). In this work, we distribute τ_I to ensure that the aforementioned ψ -averaged ρ_I^2 for all MSPs are the same. In another words, Equation 14 means that the distribution strategy is $\tau_I \propto p_I^{-1}$. Table 3 lists the values of $\tau_I / \text{Min}[\tau_I]$, which represents the distribution ratio of τ_I for a MSP with respect to the MSP with largest p_I .

Step 6- Further adjustments — The above analyses are based on the minimum integration time $\Delta\tau_I = 5$ min for each data point. A small $\Delta\tau_I$ corresponds to a high-cadence observation (small Δt_I) at a fixed τ_I , which means complicated telescope time arrangements and should be avoided in practice. Hence, we will take a further selection of $\Delta\tau_I$ and Δt_I , which may lead to adjustments of other parameters in the strategy.

The details of the further selection are shown in Figure 4, with the following factors considered. Firstly, both $\Delta\tau_I \geq 5$ min and $\Delta t_I \leq 4$ weeks (Perera et al. 2019a) are required in PTA observations, which leads to the lower limit $\tau_I \geq 5 \text{ min} \times [T_I / (4 \text{ weeks}) + 1]$. If τ_I given by Step 5 is smaller than this lower limit, the parameters T_I or τ_I should change in order to satisfy the above requirements of $\Delta\tau_I$ and Δt_I . Here we re-select T_I at $\Delta\tau_I = 5$ min and $\Delta t_I = 4$ weeks. Secondly, the value of $\Delta\tau_I$ is expected to have an upper limit, otherwise the red noise will dominate during the observation span T_I . The upper limit equals $5 \text{ min} \times (T_I^* / T_I)^{4.6}$ according to Equation 13. Furthermore, the configuration of FAST indicates that $\Delta t_I \geq 1$ day and $\Delta\tau_I \leq 1$ hour (Jiang et al. 2020). Since IPTA contains multiple telescopes, the above constraints of Δt_I and $\Delta\tau_I$ can be removed (Yi et al. 2014; Dolch et al. 2016; Perera et al. 2019b), but in reality they hold for most cases. Therefore, we adopt the constraints for both FAST-PTA and IPTA in this step. Given above, the parameters Δt_I , $\Delta\tau_I$ and T_I are reset in light of the process given in Figure 4. In our strategy, the constraints $\Delta\tau_I \geq 5$ min and $1 \text{ day} \leq \Delta t_I \leq 4$ weeks are stringently satisfied, while the other ones above are not.

Finally, we emphasize that if all the parameters T_I , $t_{I,i}$, τ_I , $\Delta\tau_I$ and Δt_I are chosen, the observation epochs of all data points for the MSP are determined.

3.3 Results

Following the above Steps 1-5, we can choose MSPs with high priority parameters p_I , and obtain their parameters T_I , $t_{I,i}$ and $\tau_I / \text{Min}[\tau_I]$, for general cases with various τ . In Table 3, we list the selected 20 MSPs with highest p_I for 5-year FAST-PTA and IPTA started at 2022.3, as well as their parameters.

In practical PTA observations, only part of the MSPs in Table 3 are needed to detect the BWM signal. If the MSPs are selected and τ is fixed, the observation epochs of all data points are obtained by the process in Figure 4. As an example, for the strategy using 7 MSPs with the highest priorities for a 5-year FAST-PTA in Table 3 and with $\tau = 500$ hours, the designed observation epochs are illustrated in Figure 5.

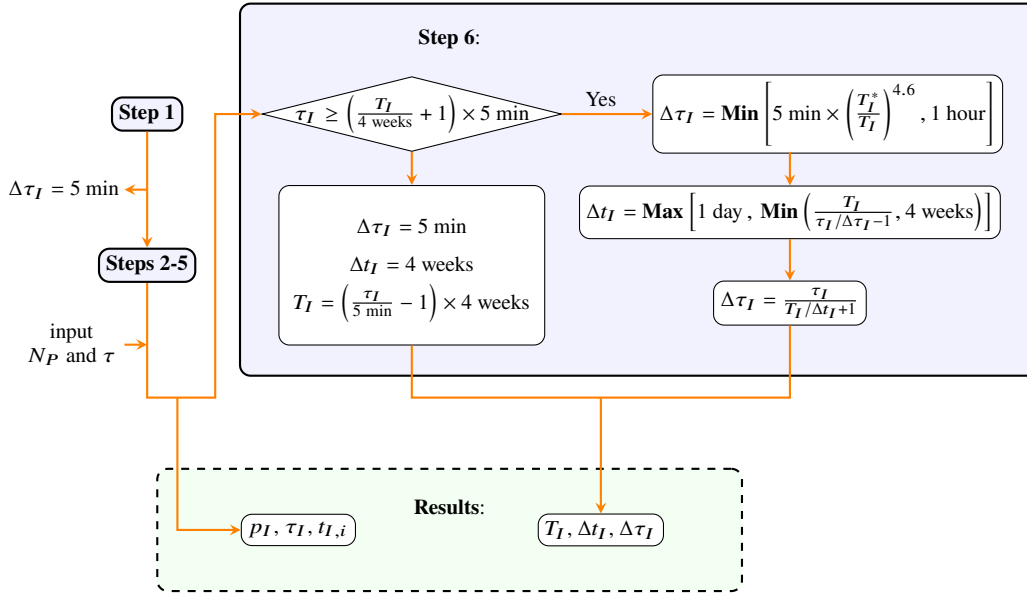


Figure 4. Process of designing the observation strategy. In particular, the details of **Step 6** are presented.

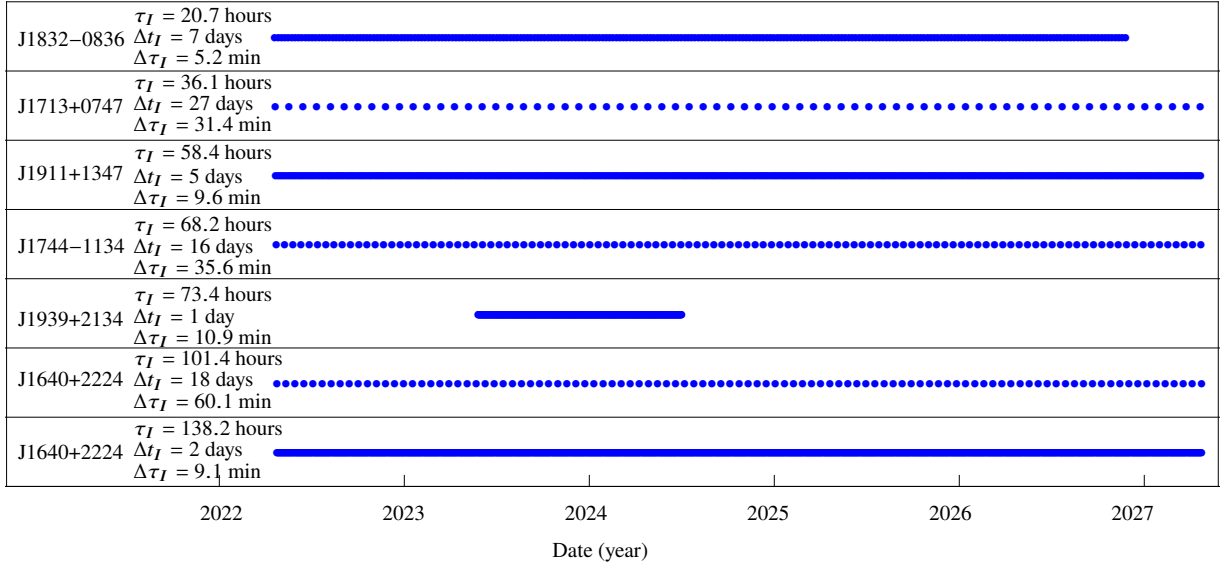


Figure 5. Illustration of the designed observation epochs for the strategy using the 7 MSPs with highest priorities in Table 3 for the FAST-PTA, with the total integration time $\tau = 500$ hours.

Furthermore, since **Step 4** only tells us to choose MSPs with the highest p_I in Table 3, the number of the MSP is still a free parameter in the strategy. In the next section, we will figure out the MSP number and thereby further select the strategies.

4 FURTHER SELECTION AND TESTS OF STRATEGIES BY SIMULATIONS

In this section, we will further select and test the strategies and investigate the prospects for detecting the BWM signal by IPTA and FAST-PTA, respectively. Since each strategy includes N_P MSPs with the highest priorities in Table 3, it will be denoted as the "best- N_P "

strategy hereafter. One goal of this part is to fix the value of N_P for the most recommended strategy.

In section 3, the uncertainties of t_m , h , ψ and $\sigma_{I,R}$ are not considered in details. Therefore, we will simulate the GW BWM signal and red noise by taking the PDFs of t_m and h given in Jiang et al. (2022) (for both Model-1 and Model-2) as well as the PDF of $\sigma_{I,R}$ given in Equation 10 and $\psi \in U[0, \pi]$. Our simulations will be shown on two aspects — the network S/Ns and the parameter-estimation errors (PEEs).

4.1 Network S/Ns: Further Selection of Strategies & Prospects for Detecting BWM Signal

In the following simulations, we select among the best- N_P strategies with $1 \leq N_P \leq 20$.

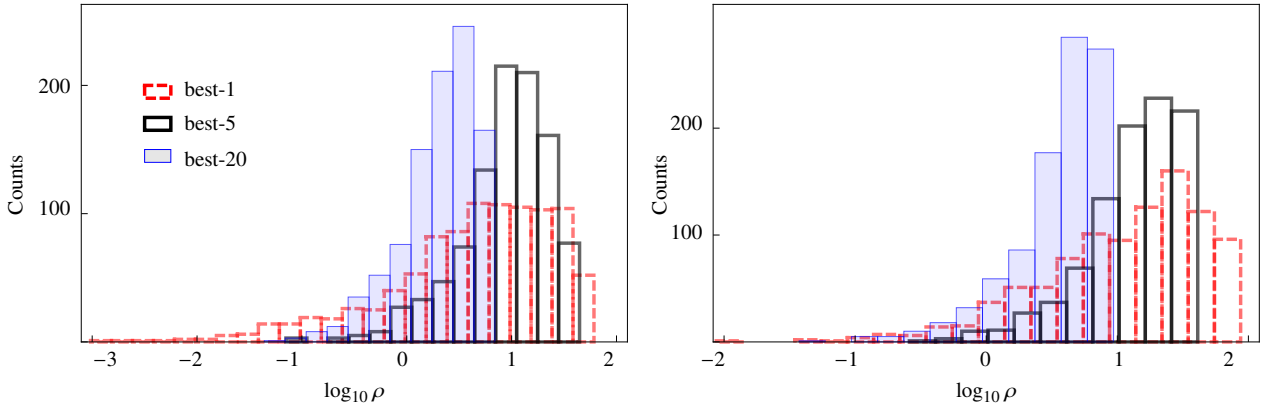


Figure 6. PDFs of network S/Ns ρ given by 1000 realizations, for a 5-year FAST-PTA observation with $\tau = 1000$ hours. The results for Model-1 are shown in the left panel and the ones for Model-2 are shown in the right panel.

We plot the PDFs of network S/Ns in Figure 6 for the best-1, best-5 and best-20 strategies in FAST-PTA. Moreover, the averaged values of ρ (actually $\sqrt{\langle \rho^2 \rangle}$) for more various strategies are listed in Table 4. The results exhibit two features. Firstly, the PDF profiles of ρ are narrower as N_P becomes larger. This is because $\sigma_{I,R}$ in our treatment is uncorrelated among different MSPs, and including more MSPs can reduce the uncertainties of ρ due to the individual red noises. Secondly, the averaged ρ decreases as N_P increases (for a fixed τ). This is due to the fact that including more MSPs means allocating τ to more MSPs with lower priorities.

However, it does not mean that the strategies with larger N_P are less favored, because the above features are not sufficient to judge the strategies. In practical observations, a significant signal requires ρ to be larger than a threshold, which is taken to be 8 in this work (Taylor et al. 2016). Therefore, the probability of $\rho > 8$ (denoted as $p(\rho > 8)$), instead of the averaged ρ , is the key figure to judge strategies, and we seek for strategies with large $p(\rho > 8)$.

Additionally, recall that in subsection 3.2, we expect ρ_I for various MSPs to have equal values. However, note that this is nearly impossible in practical observations, due to the uncertainties of parameters ψ , t_m and $\sigma_{I,R}$. For strategies with inhomogeneous ρ_I , the network S/N will be dominated by a few MSPs and may easily be biased by the individual noises of these MSPs (Chen & Wang 2022). To quantify the inhomogeneity of ρ , we introduce the parameter

$$\lambda = \frac{\text{Max}[\rho_I^2]}{\rho^2}, \quad (15)$$

which takes the value between N_P^{-1} and 1. A smaller λ represents a low ρ -inhomogeneity. Here we adopt the criterion $\lambda < 0.5$, and the probability of $\lambda < 0.5$ (denoted as " $p(\lambda < 0.5)$ ") can be taken as another important parameter to judge strategies. In details, among the strategies with almost the same $p(\rho > 8)$, the one with the largest $p(\lambda < 0.5)$ should be the most recommended one.

Our results are summarised as follows. In Table 4, we list the resulting $p(\rho > 8)$ and $p(\lambda < 0.5)$ for various strategies in IPTA and FAST-PTA. Firstly, the largest values of $p(\rho > 8)$ for FAST-PTA are $\{0.48, 0.61, 0.73\}$ for orbit Model-1 and $\{0.71, 0.82, 0.88\}$ for Model-2 with $\tau = \{500, 1000, 2000\}$ hours in 5 years, respectively. Meanwhile, the probability $p(\rho > 8)$ for IPTA is significantly smaller than the FAST-PTA result at the same condition. This means that a 5-year FAST-PTA observation has considerable potential to detect the GW BWM signal from SDSSJ1430+0323, while the IPTA is marginally capable to detect this signal in 5 years, with total in-

tegration time $\tau \leq 2000$ hours. Secondly, the largest $p(\rho > 8)$ for FAST-PTA appear at $N_P = 3 - 4$ in Model-1 and at $N_P = 3 - 6$ in Model-2. Furthermore, there are other strategies with $p(\rho > 8)$ slightly smaller than the largest values (with differences below 10%), which are also acceptable. For example, in the case $\tau = 1000$ hours, the recommended strategies include those with $N_P = 2 - 6$ for Model-1 and $N_P = 2 - 8$ for Model-2. For a general consideration with both Model-1 and Model-2, the strategies with $N_P = 2 - 6$ are recommended. Moreover, it is clear that $p(\lambda < 0.5)$ increases significantly as N_P grows. Therefore, in light of both $p(\rho > 8)$ and $p(\lambda < 0.5)$, the most recommended strategy at $\tau = 1000$ hours is the best-6 one.

4.2 Parameter-estimation Errors

In this part, we will test the capability of the recommended best-6 strategy in parameter estimation.

The parameters of the GW BWM signal can be included in a vector $\{\lambda^i\} = \{h, \psi, t_m\}$ with $i = 1, 2, 3$, and the variance of the PEE λ^i can be evaluated as $(\Delta \lambda^i)^2 = (F^{-1})^{ii}$, where $(F^{-1})^{ij}$ is the inverse of the Fisher information matrix:

$$F_{ij} = \sum_{I,n} \frac{\partial s_I(t_n)}{\partial \lambda^i} \frac{\partial s_I(t_n)}{\partial \lambda^j} \frac{1}{\sigma_{I,W}^2 + \sigma_{I,R}^2(t_n)}. \quad (16)$$

In general, one expects that the Fisher information matrix is three dimensional and contains a positive determinant ($\det[F_{ij}] > 0$). However, if the merger time t_m is earlier than the initial observation epoch $t_{I,i}$, Equation 5 will yield $\partial s_I / \partial t_m = 0$, which means t_m cannot be measured at all or equivalently $\Delta t_m = +\infty$. In this case, we use the two dimensional Fisher information matrix $\mathcal{F}_{ij} = F_{ij}$ (with $i, j = 1, 2$), and its inverse matrix is denoted as $(\mathcal{F}^{-1})^{ij}$. Given above, we evaluate the PEEs as follows: if $\det[F_{ij}] > 0$, $\Delta h^2 = (F^{-1})^{11}$, $\Delta \psi^2 = (F^{-1})^{22}$ and $\Delta t_m^2 = (F^{-1})^{33}$; if $\det[F_{ij}] = 0$, $\Delta h^2 = (\mathcal{F}^{-1})^{11}$, $\Delta \psi^2 = (\mathcal{F}^{-1})^{22}$ and $\Delta t_m^2 = +\infty$.

We notice that the probability of $t_m < t_{I,i}$ (i.e. $\Delta t_m = +\infty$) is small for Model-1, but it is not ignorable for Model-2 (as shown in Figure 7), if the PTA observation starts at 2022.3. To decrease this probability, the strategy can be optimized by combining the achieved IPTA data before $t_{I,i}$. Since we have assumed $s_I = 0$ at the initial epoch $t_{I,i}$, the timing residual template containing the achieved data should be modified to

$$s_I(t) = \begin{cases} (t - t_{I,0})\Theta(t - t_m)F_I h & t > t_{I,i} \\ [(t - t_m)\Theta(t - t_m) - (t_{I,0} - t_m)]F_I h & t < t_{I,i} \end{cases}. \quad (17)$$

Table 4. Statistical signatures for a 5-year FAST-PTA observation (upper) and a 5-year IPTA observation (lower). The results in bold face denote the largest $p(\rho > 8)$ among different strategies at a fixed τ .

FAST-PTA results for Model-1 (left) and Model-2 (right)																		
strategy	$\sqrt{\langle \rho^2 \rangle}$			$p(\rho > 8)$			$p(\lambda < 0.5)$			$\sqrt{\langle \rho^2 \rangle}$			$p(\rho > 8)$			$p(\lambda < 0.5)$		
τ / hours	500	1000	2000	500	1000	2000	500	1000	2000	500	1000	2000	500	1000	2000	500	1000	2000
best-1	15.4	21.6	28.0	0.40	0.43	0.48	0.00	0.00	0.00	26.2	34.3	48.3	0.66	0.44	0.68	0.00	0.00	0.00
best-2	13.5	19.7	25.6	0.44	0.56	0.64	0.00	0.00	0.00	23.9	33.0	43.2	0.70	0.74	0.82	0.00	0.00	0.00
best-3	12.6	17.3	22.7	0.48	0.59	0.70	0.12	0.14	0.10	20.4	28.9	38.2	0.71	0.80	0.85	0.14	0.15	0.14
best-4	11.4	16.6	22.3	0.46	0.61	0.73	0.31	0.30	0.26	17.9	25.9	36.0	0.71	0.82	0.88	0.34	0.35	0.35
best-5	11.3	15.6	21.6	0.46	0.60	0.71	0.38	0.38	0.34	16.5	23.8	33.1	0.71	0.82	0.87	0.48	0.47	0.47
best-6	10.2	14.4	19.0	0.42	0.57	0.70	0.52	0.53	0.54	15.7	22.4	31.0	0.69	0.80	0.88	0.66	0.63	0.66
best-7	9.40	12.7	18.2	0.39	0.53	0.67	0.68	0.66	0.65	14.6	20.6	28.8	0.65	0.76	0.85	0.78	0.79	0.77
best-8	8.61	12.0	17.9	0.33	0.51	0.66	0.76	0.77	0.77	13.3	19.0	26.8	0.60	0.76	0.84	0.84	0.85	0.84
best-9	7.40	10.4	14.7	0.28	0.45	0.62	0.84	0.86	0.84	11.9	16.0	22.4	0.59	0.72	0.81	0.94	0.93	0.92
best-10	6.38	8.96	12.5	0.21	0.38	0.54	0.88	0.90	0.91	9.80	13.3	19.6	0.49	0.65	0.77	0.97	0.97	0.97
best-15	3.18	4.66	6.53	0.01	0.08	0.22	0.98	0.99	0.99	4.76	7.49	10.2	0.08	0.34	0.50	1.00	1.00	1.00

IPTA results for Model-1 (left) and Model-2 (right)																		
strategy	$\sqrt{\langle \rho^2 \rangle}$			$p(\rho > 8)$			$p(\lambda < 0.5)$			$\sqrt{\langle \rho^2 \rangle}$			$p(\rho > 8)$			$p(\lambda < 0.5)$		
τ / hours	500	1000	2000	500	1000	2000	500	1000	2000	500	1000	2000	500	1000	2000	500	1000	2000
best-1	2.60	3.52	4.39	0.01	0.05	0.09	0.00	0.00	0.00	4.07	5.34	7.16	0.07	0.14	0.22	0.00	0.00	0.00
best-2	1.91	2.66	3.53	0.00	0.01	0.04	0.00	0.00	0.00	3.05	4.04	5.50	0.01	0.05	0.15	0.00	0.00	0.00
best-3	1.52	2.04	2.76	0.00	0.00	0.01	0.04	0.04	0.04	2.51	3.56	4.43	0.00	0.01	0.07	0.05	0.05	0.05

We then extend the red noise model in Equation 10 to $\hat{\sigma}_{I,R} \propto |t - t_{I,i}|^{2.3}$, making it apply for the epoch $t < t_{I,i}$.

We illustrate the results of PEEs in Figure 7. Firstly, it is clear that $\Delta h/h$ and $\Delta \psi$ have significant probabilities to achieve the precision levels of 50% and 10° , respectively, for both Model-1 and Model-2. Secondly, Δt_m can achieve the 0.5-year level with a high confidence for Model-1, but have a large probability of $\Delta t_m = +\infty$ and low probability of $\Delta t_m < 0.5$ yr in Model-2, if the FAST-PTA data are used alone. Furthermore, combining the IPTA achieved data can eliminate the probability of $\Delta t_m = +\infty$. This indicates that the IPTA achieved data is important in measuring t_m . Additionally, since the IPTA precision is not as good as FAST-PTA, the achieved 5-year data cannot improve the probability of $\Delta t_m < 0.5$ yr significantly. Hence, precisely measuring Δt_m is still a challenge for future PTA observations.

5 SUMMARY

In this article, the prospects for detecting the GW BWM signal from SDSSJ1430+0323 by IPTA and FAST-PTA are investigated. For this target signal, we present a detailed process of designing observation strategies, which includes selecting appropriate MSPs and obtaining the observation epochs for all data points. Our results show that: (i) FAST-PTA have a considerable probability to detect the BWM signal in 5 years, with total integration time ~ 500 hours; (ii) precisely measuring the merger time t_m may be a challenge for these PTA observations.

Note that our results are based on some idealized treatments, e.g. the over-estimated telescope parameters G and T_{sys} for FAST. Furthermore, our analysis of the red noise $\sigma_{I,R}$ is simple. This may lead to undesired results from the strategies, e.g. some precise MSPs have very short spans ($T \lesssim 1$ year) or their cadences are required to be very high ($\Delta t_I \lesssim 1$ day). An improvement of the analyses on $\sigma_{I,R}$ may optimize the strategies by breaking the conditions, and worth being studied in the follow-up works. Moreover, there are MSPs not con-

sidered in this work (e.g. see Kerr et al. 2020; Alam et al. 2020a,b). It indicates that our results will be updated when including these MSPs in the future.

As to the challenge in measuring Δt_m , FAST may have already accumulated precise pulsar timing data before 2022.3, for the selected MSPs in subsection 4.2. Combining the FAST achieved data is expected to further reduce the measurement error Δt_m from our results. Additionally, besides PTA observations, the GW memory may also trigger signals for the ground-based LIGO and Virgo (Yang & Martynov 2018). In particular, if LIGO and Virgo run recently, t_m can be covered in their observation time range, which provides another chance to measure it.

ACKNOWLEDGEMENTS

J. W. C. acknowledges the support from China Postdoctoral Science Foundation under Grant No. 2021M691146. Y. M. thanks Huan Yang, Yanbei Chen, Ning Jiang, Zhenwei Lv and Qingwen Wu for many helpful discussions on the SDSSJ1430 source and also acknowledges the support from the university start-up fundings of Huazhong University of Science and Technology. Y. W. gratefully acknowledges support from the National Key Research and Development Program of China (No. 2020YFC2201400), the National Natural Science Foundation of China (NSFC) under Grants No. 11973024, and Guangdong Major Project of Basic and Applied Basic Research (Grant No. 2019B030302001).

REFERENCES

- Aasi J., et al., 2015, *Classical and Quantum Gravity*, 32, 074001
 Acernese F., et al., 2014, *Classical and Quantum Gravity*, 32, 024001
 Aggarwal K., et al., 2020, *ApJ*, 889, 38
 Alam M. F., et al., 2020a, *The Astrophysical Journal Supplement Series*, 252,

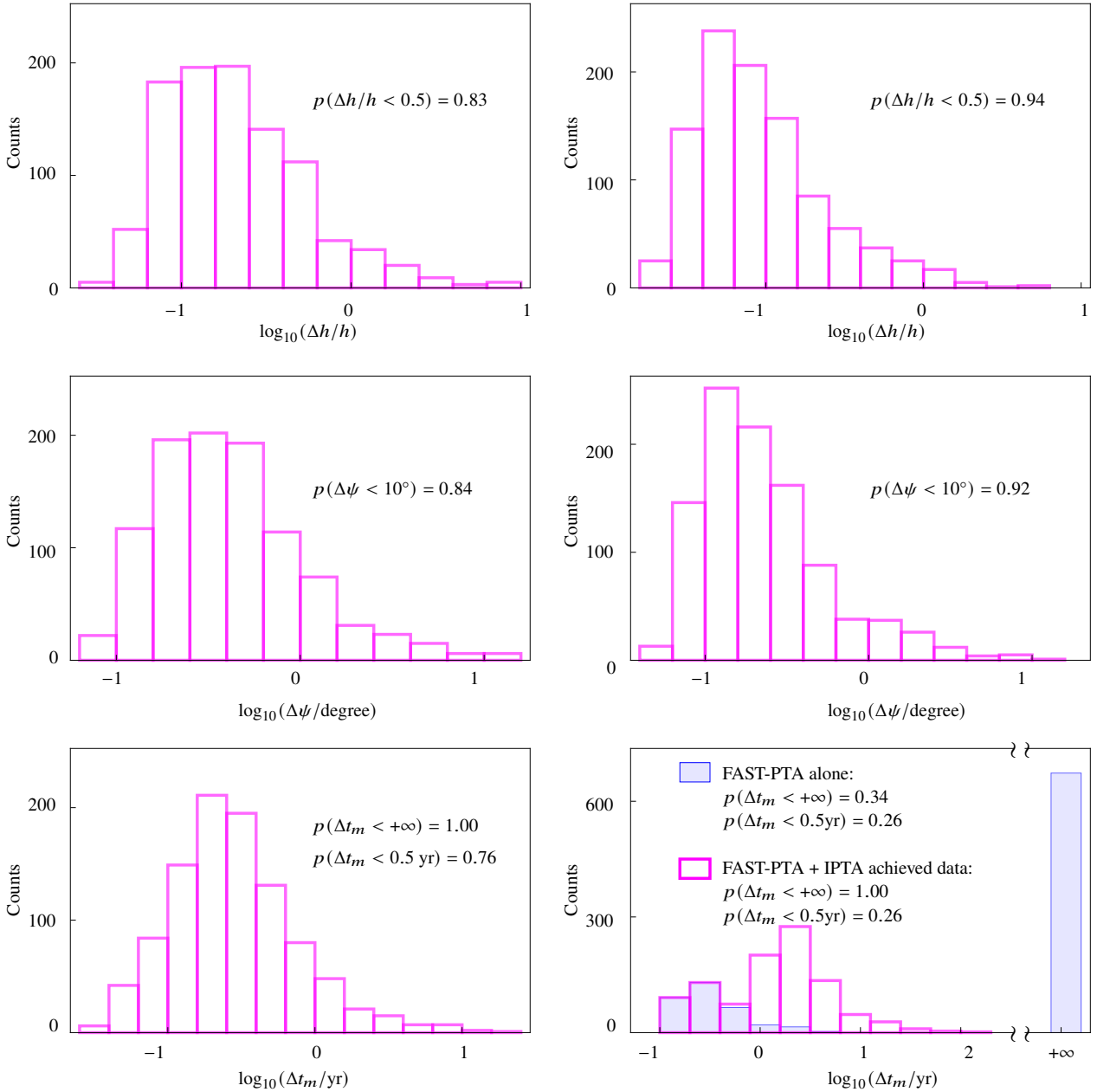


Figure 7. PDFs of PEEs for the best-6 strategy in FAST-PTA (including 5-year IPTA achieved data before $t_{I,i}$) with $\tau = 1000$ h. The results for Model-1 is shown in the left panel and for Model-2 shown in the right panel. The IPTA achieved data is assumed to be observed at a cadence $\Delta t_I = 2$ weeks.

Alam M. F., et al., 2020b, *The Astrophysical Journal Supplement Series*, 252, 5
Amaro-Seoane P., et al., 2017, Laser Interferometer Space Antenna, doi:10.48550/ARXIV.1702.00786, <https://arxiv.org/abs/1702.00786>
Arzoumanian Z., et al., 2015, *ApJ*, 810, 150
Berti E., Cardoso V., Will C. M., 2006, *Phys. Rev. D*, 73, 064030
Blanchet L., Damour T., 1992, *Phys. Rev. D*, 46, 4304
Chen J.-W., Wang Y., 2022, Parameter-Estimation Biases for Eccentric Supermassive Binary Black Holes in Pulsar Timing Arrays: Biases Caused by Ignored Pulsar Terms, doi:10.48550/ARXIV.2203.05280, <https://arxiv.org/abs/2203.05280>
Christodoulou D., 1991, *Phys. Rev. Lett.*, 67, 1486
Damour T., 2008, *International Journal of Modern Physics A*, 23, 1130
Danzmann K., 1997, *Classical and Quantum Gravity*, 14, 1399
Desvignes G., et al., 2016, *Monthly Notices of the Royal Astronomical Society*, 458, 3341

Dolch T., et al., 2016, *Journal of Physics: Conference Series*, 716, 012014
Favata M., 2009a, *Phys. Rev. D*, 80, 024002
Favata M., 2009b, *Journal of Physics: Conference Series*, 154, 012043
Favata M., 2009c, *The Astrophysical Journal*, 696, L159
Harry G. M., 2010, *Classical and Quantum Gravity*, 27, 084006
Hobbs G., 2013, *Classical and Quantum Gravity*, 30, 224007
Hobbs G., et al., 2010, *Classical and Quantum Gravity*, 27, 084013
Hobbs G., Dai S., Manchester R. N., Shannon R. M., Kerr M., Lee K.-J., Xu R.-X., 2019, *Research in Astronomy and Astrophysics*, 19, 020
Hu W.-R., Wu Y.-L., 2017, *National Science Review*, 4, 685
Jiang P., et al., 2020, *Research in Astronomy and Astrophysics*, 20, 064
Jiang N., et al., 2022, Tick-Tock: The Imminent Merger of a Supermassive Black Hole Binary, doi:10.48550/ARXIV.2201.11633, <https://arxiv.org/abs/2201.11633>
Joshi B. C., Arumugasamy P., Bagchi M., Bandyopadhyay D., Basu A., et al., 2018, *J. Astrophys. Astron.*, 39
Kerr M., et al., 2020, *Publications of the Astronomical Society of Australia*,

- 37, e020
- Kramer M., Champion D. J., 2013, *Classical and Quantum Gravity*, 30, 224009
- Lam M. T., et al., 2016, *The Astrophysical Journal*, 834, 35
- Lee K. J., 2016, in Qain L., Li D., eds, *Astronomical Society of the Pacific Conference Series Vol. 502, Frontiers in Radio Astronomy and FAST Early Sciences Symposium 2015*. p. 19
- Luo J., et al., 2016, *Classical and Quantum Gravity*, 33, 035010
- Manchester R. N., 2013, *Classical and Quantum Gravity*, 30, 224010
- Manchester R. N., Hobbs G. B., Teoh A., Hobbs M., 2005, *The Astronomical Journal*, 129, 1993
- Manchester R. N., et al., 2013, *Publications of the Astronomical Society of Australia*, 30, e017
- McLaughlin M. A., 2013, *Classical and Quantum Gravity*, 30, 224008
- Nan R., et al., 2011, *International Journal of Modern Physics D*, 20, 989
- Payne P. N., 1983, *Phys. Rev. D*, 28, 1894
- Perera B. B. P., et al., 2019a, *Monthly Notices of the Royal Astronomical Society*, 490, 4666
- Perera B. B. P., et al., 2019b, *Monthly Notices of the Royal Astronomical Society*, 490, 4666
- Pshirkov M. S., Baskaran D., Postnov K. A., 2010, *Monthly Notices of the Royal Astronomical Society*, 402, 417
- Ransom S., et al., 2019, in *Bulletin of the American Astronomical Society*. p. 195 ([arXiv:1908.05356](https://arxiv.org/abs/1908.05356))
- Rathnasree N., Rankin J. M., 1995, *ApJ*, 452, 814
- Shannon R. M., Cordes J. M., 2010, *The Astrophysical Journal*, 725, 1607
- Siemens X., Ellis J., Jenet F., Romano J. D., 2013, *Classical and Quantum Gravity*, 30, 224015
- Taylor S. R., Huerta E. A., Gair J. R., McWilliams S. T., 2016, *The Astrophysical Journal*, 817, 70
- Thorne K. S., 1992, *Phys. Rev. D*, 45, 520
- Wang Y., 2015, in *Journal of Physics Conference Series*. p. 012019 ([arXiv:1505.00402](https://arxiv.org/abs/1505.00402)), doi:10.1088/1742-6596/610/1/012019
- Wang J. B., et al., 2015, *Monthly Notices of the Royal Astronomical Society*, 446, 1657
- Yang H., Martynov D., 2018, *Phys. Rev. Lett.*, 121, 071102
- Yi S., Stappers B. W., Sanidas S. A., Bassa C. G., Janssen G. H., Lyne A. G., Kramer M., Zhang S.-N., 2014, *Monthly Notices of the Royal Astronomical Society*, 445, 1245
- van Haasteren R., Levin Y., 2010, *Monthly Notices of the Royal Astronomical Society*, 401, 2372

This paper has been typeset from a $\text{\TeX}/\text{\LaTeX}$ file prepared by the author.